

# Shear-Selected Clusters From the Deep Lens Survey III: Masses from Weak Lensing

Alexandra Abate<sup>1</sup>, D. Wittman<sup>2</sup>, V. E. Margoniner<sup>2</sup>, S. L. Bridle<sup>3</sup>, Perry Gee<sup>2</sup>, J. Anthony Tyson<sup>2</sup>, Ian P. Dell'Antonio<sup>4</sup>

## ABSTRACT

We present weak lensing mass estimates of seven shear-selected galaxy cluster candidates from the Deep Lens Survey. The clusters were previously identified as mass peaks in convergence maps of 8.6 deg<sup>2</sup> of  $R$  band imaging, and followed up with X-ray and spectroscopic confirmation, spanning a redshift range 0.19—0.68. Most clusters contained multiple X-ray peaks, yielding 17 total mass concentrations. In this paper, we constrain the masses of these X-ray sources with weak lensing, using photometric redshifts from the full set of  $BVRz'$  imaging to properly weight background galaxies according to their lensing distance ratios. We fit both NFW and singular isothermal sphere profiles, and find that the results are insensitive to the assumed profile. We also show that the results do not depend significantly on the assumed prior on the position of the mass peak, but that this may become an issue in future larger samples. The inferred velocity dispersions for the extended X-ray sources range from 250—800 km s<sup>-1</sup>, with the exception of one source for which no lensing signal was found. This work further establishes shear selection as a viable technique for finding clusters, but also highlights some unresolved issues such as determination of the mass profile center without biasing the mass estimate, and fully accounting for line-of-sight projections. A follow-up paper will examine the mass-X-ray scaling relations of these clusters.

*Subject headings:* gravitational lensing — surveys — galaxies: clusters: general

---

<sup>1</sup>Laboratoire de l'Accélérateur Linéaire, IN2P3-CNRS, Université de Paris-Sud, BP. 34, 91898 Orsay Cedex, France; abate@lal.in2p3.fr

<sup>2</sup>Physics Department, University of California, Davis, CA 95616; dwittman@physics.ucdavis.edu

<sup>3</sup>Department of Physics, University College London, Gower Street, London WC1E 6BT

<sup>4</sup>Physics Department, Brown University, Providence, RI 02912

## 1. Introduction

Clusters of galaxies are the largest virialized structures in the universe. Tracing the distribution of these structures as a function of cosmic time provides a measurement of the growth of structure and is therefore a sensitive probe of dark energy (Haiman et al. 2001; Battye & Weller 2003). This method of constraining dark energy requires accurate cluster mass estimates as well as unbiased samples of clusters selected over a broad range in mass and redshift (and with a well-defined selection function). There are two well-established selection techniques—optical detection of the member galaxies (Gal 2008) and X-ray detection of the hot intracluster gas (Rosati et al. 2002)—and two newer techniques— weak gravitational lensing (Wittman et al. 2001; Hennawi & Spergel 2005) and the Sunyaev-Zeld’ovich effect (SZE, Carlstrom et al. 2002), in which the cosmic microwave background is modified during its passage through the large potential wells associated with the intracluster medium.

Each method has its strengths and weaknesses. Optical detection is capable of finding even poor clusters with relatively little observational resources, but its cluster selection function is the least well understood because the connection between mass (whose clustering is predictable) and galaxies is not well understood. X-ray selection is the least affected by line-of-sight projections because X-ray emissivity scales as the square of the local density, but by the same token clumpiness within the cluster changes the observable at a constant mass. SZE has the advantage of being nearly redshift-independent, but large SZE surveys are not yet available. Lensing selection is based most directly on mass, but it is observationally difficult because galaxies *behind* the cluster must be imaged well enough to infer the shear induced by the cluster. Whatever method is used to select the clusters, the next step is to infer cluster masses. Here the nonlensing methods depend on assumptions about the dynamical state of the cluster, and lensing may be useful for calibrating the masses of subsamples. However, this is observationally easier than determining the lensing masses of individual clusters because subsamples may be stacked (Johnston et al. 2007; Rozo et al. 2008).

In this paper we determine lensing masses of shear-selected clusters, so hereafter we focus on the issues involved in shear selection and lensing mass determination. The weak lensing shear signal induced by a cluster is a function of its mass profile and its redshift relative to the background source galaxies being sheared, and is independent of the nature of the matter and of its dynamical or physical state. However weak lensing mass estimates do suffer from line-of-sight projections: structure along the line-of-sight could artificially boost the lensing signal or cause false positive detections. In addition poor knowledge of the source redshift distribution, as is often the case with only photometric redshift estimates, limits the accuracy of the mass estimate. We describe our choices in dealing with these issues as they

arise later in the paper.

This paper is organized as follows. We describe the selection of and previous work on these clusters in §2. In §3, we summarize the data and its processing to the point of shear and photometric redshift catalogues. In §4, we describe the fitting procedure used to estimate the masses. We present the results in §5, and summarize and discuss the implications in §6. Throughout this paper we assume a flat universe with  $\Omega_m = 0.3$  and Hubble constant  $H_0 = 70 \text{ km s}^{-1} \text{ Mpc}^{-1}$ .

## 2. Cluster Selection and Previous Work

The Deep Lens Survey (DLS: Wittman et al. 2002) is a deep  $20 \text{ deg}^2$   $BVRz'$  survey conducted with the Mosaic imagers (Muller et al. 1998) on the CTIO and KPNO 4-m telescopes, with nominal exposure times of 18 ks in  $R$  and 12 ks in the remaining bands. The clusters in this paper were shear-selected from the  $8.6 \text{ deg}^2$  which had at least 9 ks coverage in  $R$  band as of March 2002. Here we briefly summarize their selection and spectroscopic and X-ray followup. We refer readers to Wittman et al. (2006) for much more detail.

Wittman et al. (2006) ranked the shear peaks and then folded multiple peaks within a  $16'$  *Chandra* ACIS-I field of view into candidate fields for X-ray followup. The top eight candidate fields were observed for 20 ks each with ACIS-I in *Chandra* AO4, with the exception of Abell 781, which had archival *Chandra* data. Wittman et al. (2006) also obtained Keck and CTIO Hydra spectroscopy of likely cluster members, for redshift confirmation and to identify any line-of-sight projections. Redshifts were found to range from 0.19 to 0.68. Only one candidate (Candidate 5) was found to be a line-of-sight projection, on the basis of the spectroscopy and the absence of any detected X-ray emission. At the same time, most other candidates were found to contain multiple X-ray-emitting clumps, even where only one shear peak was present. In some cases, the additional extended X-ray sources correspond to extensions of the convergence map contours away from the main peak. See figures 8 to 12 and 14 to 17 in Wittman et al. (2006) where the multiband optical imaging of each candidate, with convergence maps and X-ray contours overlaid, were presented. The maps of Wittman et al. (2006) were not well suited to resolving multiple peaks because of the heavy smoothing, as the kernel described by Wittman et al. (2006) is approximately equal to a Gaussian with  $\sigma = 6.25'$ . In this paper, we use the shear data to fit a mass model to each extended X-ray source. This eliminates the need for smoothing, so we expect this process to yield mass estimates even where the original maps did not show a clear peak. We also use improved shear data as described below.

Two of the candidates have already been published in further detail. Wittman et al. (2003) reported the spectroscopy and strong lensing arc of Candidate 8 at  $z = 0.68$ . Sehgal et al. (2008) conducted a detailed X-ray and shear-fitting analysis of Candidate 1 at  $z = 0.30$  (Abell 781; note that the candidates are ranked by shear signal, so that Abell 781 was the top candidate). Abell 781 has multiple clumps which were fit simultaneously so as not to bias the mass estimates for individual clumps. In this paper, we present simultaneous mass profile fits to all seventeen X-ray-emitting clumps in all the candidate fields, as well as an overall fit to each candidate field. We repeat the fitting of Abell 781 because Sehgal et al. (2008) used a completely different code and a slightly inferior version of the data, and we show that the two sets of results are consistent.

### 3. Data

The DLS includes five widely separated  $2^\circ$  by  $2^\circ$  fields, labeled F1 through F5. F1 and F2 are in the northern hemisphere and were observed with the Mosaic camera (Muller et al. 1998) on the Kitt Peak Mayall 4-m telescope, while the remaining fields are in the south and were imaged with Mosaic II on the Cerro Tololo Blanco 4-m telescope. Each field is divided into a  $3 \times 3$  grid of  $40'$  by  $40'$  subfields. The imaging data set for each subfield consists of 20 dithered exposures in each of four bands ( $BVRz'$ ), with each exposure lasting 900 s in  $R$  and 600 s in the other bands. Observations were done in  $R$  when the seeing was better than  $0.9''$  FWHM, and galaxy shapes were measured in  $R$  only. Wittman et al. (2002) contains full details of the survey design. As mentioned above, the original candidate selection was done on the subfields (totaling  $8.6 \text{ deg}^2$ ) for which at least 9 ks (10 exposures) of  $R$  band imaging had been completed by March 2002. In this paper, we use the full imaging data set, so the data are deeper, and in some cases may extend to a larger distance from the candidate.

For each filter and subfield, the 20 exposures were combined into a single stacked image using custom software as described in Wittman et al. (2006). The original images are  $8192 \times 8192$  pixels, with gaps between the eight CCDs and a pixel size which varies over the field but averages to about  $0.26''$ . The stacked images are  $10000 \times 10000$  pixels with a uniform pixel scale of  $0.257''$  and with no gaps, cosmic rays, or satellite trails. The stacked point-spread function (PSF) size ranges from  $0.8\text{-}0.9''$  in  $R$  and from  $0.9\text{-}1.2''$  in the other filters, depending on field and subfield. Wittman et al. (2006) contains many more details on the stacking procedure. A minor improvement over the Wittman et al. (2006) and Sehgal et al. (2008) processing is the use of a Lanczos-windowed sinc function for pixel interpolation,

rather than a truncated sinc function.<sup>1</sup>

Cataloging and photometric redshift estimation proceeded much as in Sehgal et al. (2008). We ran SExtractor (Bertin & Arnouts 1996) on the stacked images in dual-image mode by detecting in  $R$  and measuring in each of  $BVRz'$ . We determined shapes of galaxies using the “VM” method described in Heymans et al. (2006). This is a partial implementation of Bernstein & Jarvis (2002) which does not give higher weight to lower-ellipticity sources, so it should not lose accuracy in high-shear regions as does the full Bernstein & Jarvis (2002) method. We apply a correction factor of  $\frac{1}{0.89}$  to the VM shears, based on performance in the blind analysis of simulations presented by Heymans et al. (2006) (corrected for stellar contamination which was present in those simulations but not in these data), and we fold a 10% shear calibration systematic uncertainty into the cluster mass uncertainties.

We used BPZ (Benítez 2000) to estimate photometric redshifts, using the HDF prior and template tweaking as described in Margoniner & Wittman (2008) (based on the algorithm designed by Ilbert et al. (2006)). When compared against 328 galaxies with spectroscopic redshifts in the NASA/IPAC Extragalactic Database (*not* used in the template tweaking), the rms photometric redshift error per galaxy is  $0.047(1+z)$ , with a bias of  $0.017(1+z)$  and no catastrophic outliers over the redshift range 0.02–0.70 (Sehgal et al. 2008). However, these are relatively bright galaxies, and we expect that performance is worse for the more typical faint galaxies used in the shear fitting. We address that concern in §4.2 below.

For each subfield, we matched the shape and photometric redshift catalogs, eliminating galaxies which failed one or the other procedure, and then applied masks around bright stars. We also cut sources with extremely large or exactly zero errors on the measured ellipticity, indicating a problem with the ellipticity measurement; saturated sources; and sources with a photometric redshift greater than 1.6. We imposed the latter cut because photometric redshift performance is predicted to be poor after the 4000 Angstrom break is shifted through the  $z'$  filter, and we have no spectroscopy in that redshift range to evaluate how it degrades. Finally, we stitched together the nine subfields in each field, checking that object attributes in the overlap regions were consistent and that no objects were duplicated.

---

<sup>1</sup>Lanczos interpolation is often used in popular packages such as SWarp, but the rationale is not widely known. Sinc interpolation has the virtue of being *exact* for band-limited data (e.g. Bracewell 2000), but it converges very slowly. Simple truncation, as was done for the Wittman et al. (2006) images, leads to artifacts; one can see this by considering the effects in Fourier space of a top-hat window in pixel space. The Lanczos- $n$  window smoothly truncates the sinc function at its  $n$ th zero by multiplying it by another sinc function whose first zero occurs there. This also provides the useful property that the derivative of the interpolation kernel is zero at its edge.

#### 4. Fitting procedure

The observed reduced shear components,  $g_1^o$  and  $g_2^o$ , are calculated from the measured ellipticities of the source galaxies  $e_1$  and  $e_2$  by dividing by the shear responsivity correction  $R_s$ :  $g_i^o = e_i/R_s$ . We fit a model for the mass distribution of each cluster to the observed shear components, taking into account the full three-dimensional position of each source galaxy (r.a., dec., photo-z).

We refer to each shear-selected cluster as a candidate and each X-ray detection within the vicinity of a candidate position as a “clump”. The X-ray positions give a better indication of a cluster center than the shear peak position because the X-ray centroids are more precise statistically. *Chandra* has 0.5'' angular resolution, while the convergence maps have  $> 1'$  resolution. We number the candidates from 1 to 8 and label the X-ray clumps in their vicinity with lowercase letters. Where there are multiple shear peaks (which have X-ray confirmation) within what could be considered a single candidate, we label them with uppercase letters. For each clump the r.a. and dec. positions are given by the X-ray position, and the redshift is given by a spectroscopic measurement, except for clumps 2b, 2c and 7c. The photometric redshifts of these clumps are consistent with the spectroscopic redshifts of the main clump in their respective fields, so in these cases we use the main clump spectroscopic redshift. The information on the clusters according to the labelling described above is presented in Table 1. Note that Table 2 of Wittman et al. (2006) contains a typographical error in the position of Candidate 1; the correct position for the candidate field is 09:20:50 +30:27:44 (J2000).

In addition to the quality cuts mentioned in Section 3 we remove any sources which have redshifts less than  $z_c + 0.2$ , where  $z_c$  is the redshift of the cluster. This is to avoid cluster member contamination in the sample of source galaxies. Cluster members scattering to higher redshifts would reduce the observed shear. When the fit applies to multiple clumps we take  $z_c$  to be the redshift of the highest redshift clump. The effect of the minimum photometric redshift cut on cluster member contamination is shown by Figure 1 for clump 1a; the same plot for the other clusters yields similar results. The number density as a function of radius is plotted before and after applying a minimum photometric redshift cut on the source catalogue. When there is no minimum photometric redshift (black stars) there is clear cluster member contamination at radii less than 10 arcminutes. When the minimum photometric redshift cut is applied (red circles) the number density is approximately flat with radius as shown by the fitted red dotted line. The gradient of the red dotted line is not significantly different from zero given the size of the scatter of the red circles. This implies there is no cluster member contamination, so no additional radius cut or correction is required.

We use only sources that are within 30' of a profile center, partly for computational

Table 1: Top 8 shear-selected clusters from DLS. The clumps within each candidate are listed in order of decreasing X-ray flux.

Cand.	Shear peak info.			Clump info.			
	Field	R.A. <sup>a</sup>	Dec. <sup>a</sup>	Clump	R.A. <sup>b</sup>	Dec. <sup>b</sup>	$z^c$
1A	F2	09:20:27	+30:30:44	a	9:20:26.4	+30:29:39	0.302 (1)
1B		09:20:50	+30:27:44	b	9:20:53.0	+30:28:00	0.291 (1)
1C		09:21:11	+30:27:39	c	9:21:10.3	+30:27:52	0.427 (1)
				d	9:20:11.1	+30:29:55	0.302 (1)
2	F3	05:22:17	-48:20:10	a	05:22:15.6	-48:18:17	0.296 (3)
				b	05:21:59.6	-48:16:06	0.296 (2)
				c	05:21:47.6	-48:21:24	0.296 (2)
				d	05:22:46.6	-48:18:04	0.210 (5)
3	F4	10:49:41	-04:17:44	a	10:49:37.9	-04:17:29	0.267 (3)
				b	10:49:50.7	-04:13:38	0.068 (4)
4	F4	10:54:08	-05:49:44	a	10:54:14.8	-05:48:50	0.190 (4)
5	F5	14:02:12	-10:28:14	-	-	-	-
6	F5	14:02:03	-10:19:44	a	14:01:59.7	-10:23:02	0.427 (5)
7	F2	09:16:00	+29:31:34	a	09:15:51.8	+29:36:37	0.530 (5)
				b	09:16:01.1	+29:27:50	0.531 (5)
				c	09:15:54.4	+29:33:16	0.530 (2)
8	F4	10:55:12	-05:03:43	a	10:55:10.1	-05:04:14	0.680 (6)
				b	10:55:35.6	-04:59:31	0.609 (5)

<sup>a</sup>Position of shear peak in DLS.

<sup>b</sup>Position of X-ray peak in Chandra follow-up.

<sup>c</sup>Redshift sources: (1) Geller et al. 2005; (2) Wittman et al. 2006, photometric; (3) Wittman et al. 2006: CTIO 4-m/Hydra; (4) Colless et al. 2001: 2dF; (5) Wittman et al. 2006: Keck/LRIS; (6) Wittman et al. 2003

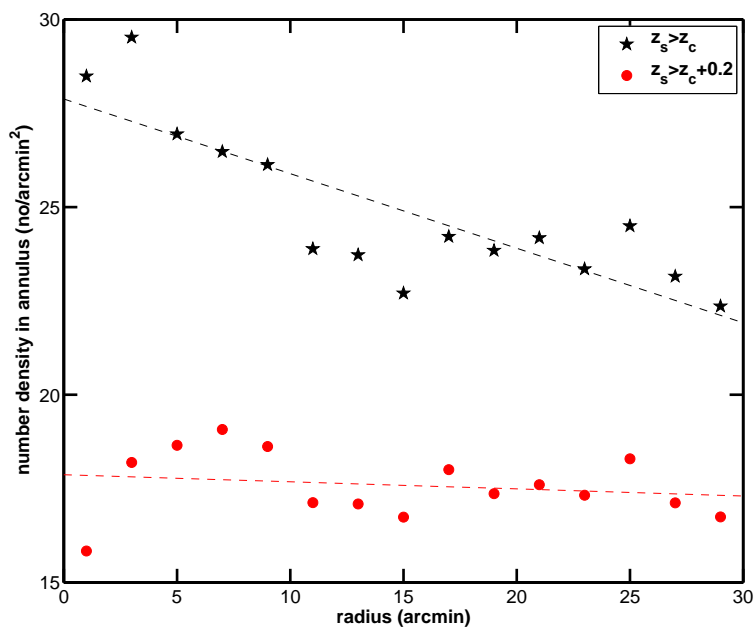


Fig. 1.— Cluster member contamination illustrated by the number density as a function of radius for clump 1a. The result is typical of the rest of the clusters. The number density is plotted before (black stars) and after (red circles) applying a minimum photometric redshift cut on the source catalogue. The minimum photometric redshift cut alone is adequate in removing cluster member contamination.



efficiency but mostly because sources at large radii will contain very little information on the cluster mass and be influenced by other nearby masses (see Figure 8 of Johnston et al. 2007). Following Hoekstra et al. (2002) and Cypriano et al. (2004) we additionally remove sources within  $1'$  of a cluster center. This is because in the most inner regions the mass densities could be closer to the critical value, leading to unmodeled strong lensing effects.

For each model the best-fit parameters were obtained through evaluation of the  $\chi^2$  statistic, defined as

$$\chi^2 = \sum_i \left( \frac{g_1^p - g_1^o}{\sigma_{g_1}} \right)_i^2 + \left( \frac{g_2^p - g_2^o}{\sigma_{g_2}} \right)_i^2 \quad (1)$$

where  $g_1^o$  and  $g_2^o$  are the measured shears. In Eq. 1 the  $i$  denotes the different source galaxies. The advantage of this approach is that it avoids data binning. We also use index  $m$  to distinguish between the two ellipticity components so  $g_m^p$  is the predicted  $g_1$  or  $g_2$  component for the source galaxy given a certain mass model. The error  $\sigma_{g_m}$  is the error on the ellipticity component which comes from the shape noise ( $\sigma_{SN}$ ), the measurement noise ( $\sigma_m$ ) and the photometric redshift noise ( $\sigma_{\gamma z}$ , see Section 4.2 below) added in quadrature:  $\sigma_{g_m}^2 = \sigma_{SN}^2 + \sigma_m^2 + \sigma_{\gamma z}^2$ . A separate measure of  $\sigma_m$  for is used each galaxy.

The shape noise is estimated by finding the standard deviation of  $g_m$  values which have small measurement error (i.e.  $\sigma_m < 0.002$ , leaving about 700 galaxies to compute the estimate). Then the shape noise  $\sigma_{SN}$  is the average value estimated from  $g_1$  and  $g_2$  and we find  $\sigma_{SN} \sim 0.25$ .

The predicted  $g_1^p$  and  $g_2^p$  are calculated from the reduced shear:

$$g = \frac{\gamma}{1 - \kappa} \quad (2)$$

where the form of  $\gamma$  and  $\kappa$  depends on the model (see Section 4.1 below). Then the prediction for each shear component  $g_1^p$  and  $g_2^p$  for a circularly symmetric distribution are:

$$\begin{aligned} g_1^p &= -g \cos 2\phi \\ g_2^p &= -g \sin 2\phi \end{aligned} \quad (3)$$

where  $\phi$  is the angle subtended at the cluster center between the positive x-axis and the line from the cluster center to the position of the source galaxy.

#### 4.1. Mass Models

We consider two different mass models, the singular isothermal sphere (SIS) and the Navarro, Frenk and White (NFW) profiles. The advantage of the SIS profile is that it has a

very simple form and only one free parameter, the velocity dispersion  $\sigma_v$ . The NFW profile has two free parameters, the concentration  $c_c$  and  $M_{200}$ , the mass within the radius at which the density is 200 times the critical density in the universe.

The SIS profile is the density distribution found after solving the Boltzmann equations describing gravitational equilibrium of an isothermal gas. For the SIS profile the convergence and the shear are given by

$$\kappa = \gamma = \frac{1}{2} \frac{\theta_E}{|\theta|} \quad (4)$$

where  $\theta_E$  is the Einstein radius, which is related to the one-dimensional velocity dispersion of the isothermal sphere by

$$\theta_E = \frac{4\pi\sigma_v^2}{c^2} \frac{D_{ds}}{D_s} \quad (5)$$

$\sigma_v$  is the velocity dispersion (the mass proxy),  $c$  the speed of light,  $D_{ds}$  is the angular diameter distance from the lensing mass to the source galaxies, and  $D_s$  is the angular diameter distance from the observer to the source galaxies. The shear from the SIS profile diverges at small projected radii, but the enclosed mass does not. With the  $1'$  cut imposed for other reasons (§4), we do not attempt to fit these regions directly in any case and therefore do not encounter numerical stability problems.

The NFW profile is the distribution of dark matter predicted from N-body simulations (Navarro et al. 1997). The characteristic radius of a cluster is defined as  $r_s = r_{200}/c_c$ , and the projected radius relative to the center of the lens as  $R$ . The analytic expression for the shear as a function of  $x \equiv R/r_s$  is given by (Wright & Brainerd 2000):

$$\begin{aligned} & \frac{r_s \delta_c \rho_{cr}}{\Sigma_{cr}} A(x) & (x < 1) \\ \gamma(x) = & \frac{r_s \delta_c \rho_{cr}}{\Sigma_{cr}} \left[ \frac{10}{3} + 4 \ln \left( \frac{1}{2} \right) \right] & (x = 1) \\ & \frac{r_s \delta_c \rho_{cr}}{\Sigma_{cr}} B(x) & (x > 1) \end{aligned} \quad (6)$$

where the functions  $A(x)$  and  $B(x)$  depend only on the dimensionless radius  $x$  (see Wright & Brainerd 2000, for their explicit form),  $\delta_c$  is a characteristic overdensity for the halo,  $\rho_{cr}$  is the critical density of the universe at the redshift of the cluster and  $\Sigma_{cr}$  is the critical surface mass density,

$$\Sigma_{cr} = \frac{c^2}{4\pi G} \frac{D_s}{D_d D_{ds}} \quad (7)$$

where  $D_d$  is the angular diameter distance from the observer to the lensing mass. The convergence  $\kappa$  is the ratio of the local value of the surface mass density to the critical surface mass density,  $\kappa = \Sigma(x)/\Sigma_{cr}$ , where  $\Sigma(x)$  is given by (Wright & Brainerd 2000):

$$\begin{aligned} & \frac{2r_s\delta_c\rho_{cr}}{(x^2-1)} \left[ 1 - \frac{2}{\sqrt{1-x^2}} \operatorname{arc tanh} \sqrt{\frac{1-x}{1+x}} \right] \quad (x < 1) \\ \Sigma(x) = & \frac{2r_s\delta_c\rho_{cr}}{3} \quad (x = 1) \\ & \frac{2r_s\delta_c\rho_{cr}}{(x^2-1)} \left[ 1 - \frac{2}{\sqrt{x^2-1}} \operatorname{arctan} \sqrt{\frac{x-1}{1+x}} \right] \quad (x > 1). \end{aligned} \tag{8}$$

The dependence on the halo mass enters Eq. 8 and Eq. 6 mainly through the scale radius  $r_s$ , and the dependence on the concentration mainly through  $r_s$  and  $\delta_c$ . There is a weak dependence on cosmology through  $\rho_{cr}$ ,  $\Sigma_{cr}$  and  $x$ .

We perform the fitting in two ways:

- (i) We fit one mass profile to each candidate. The high resolution of the X-ray data means that the X-ray position is a better estimator of the cluster center than the shear peak position. Therefore we vary the cluster center around the X-ray position; the cluster center is a free parameter. The X-ray position will usually be decentered slightly from the observed mass peak because of noise peaks superimposed on the mass distribution (see Clowe et al. 2006, and references within). Therefore even using a well resolved shear peak position could cause a systematic overestimate of the mass. If the offset is real, for example due to current or recent merging of clusters, then using the X-ray position would result in a systematic underestimate of the mass. At the same time, marginalizing over central positions over a large area biases the mass low. This is because fitting a profile positioned far from the true mass peak results in the prediction of a very low mass. We have confirmed this effect using simulated data.

We therefore apply a prior on the cluster’s X-ray/lensing offset, and turn to the literature for guidance on the size of the prior. Smith et al. (2005) examined this question observationally for ten massive clusters with high-resolution lensing maps from *Hubble Space Telescope* observations. In this case, the X-ray/lensing offset is much less affected by noise compared to the DLS clusters, which are less massive and have lower-resolution lensing constraints due to lower background source density. Smith et al. (2005) found offsets ranging from 0–120 kpc, with an rms of 38 kpc. Koester et al. (2007) examined 76 clusters identified in Sloan Digital Sky Survey photometric data and found a typical offset of  $57h^{-1}$  kpc between the X-ray centroid and the brightest cluster galaxy (BCG). For  $h = 0.7$ , the value assumed throughout this paper, this is roughly double the separation found by Smith et al. (2005). Assuming the BCG lies close to the bottom of the gravitational potential, the Koester et al. (2007) result should be more representative of our data because our clusters are of comparably modest richness.

We therefore adopt a prior of the form

$$P = \mathcal{N}e^{-\frac{r^2}{2\sigma_r^2}} \quad (9)$$

where  $r$  is the angular separation on the sky between the highest flux X-ray peak position and the cluster center position,  $\sigma_r$  is the angular separation of a  $57h^{-1} = 81$  kpc distance at the redshift of the cluster. We then marginalize over the cluster center positions.

- (ii) In the second approach, we simultaneously fit all the X-ray clumps in the vicinity of a candidate, to eliminate any influence one cluster may have on the inferred mass of another cluster. The shears from different clusters add linearly because they are small, so the predicted shear for the multi-profile fit is  $g_m^p = g_{ma}^p + g_{mb}^p + g_{mc}^p + \dots$ , summing up all the predicted reduced shears from each cluster. we use the exact X-ray peak positions as the profile centers in this fit. The  $g_{ma}^p$  etc are calculated as before (Eqs. 2 and 3) but the values of e.g. the distance ratios,  $\phi$  and  $|\theta|$  (used to calculate  $g$ ) will depend upon the clump in question.

## 4.2. Photometric Redshift Errors

Each of the source galaxies has a photometric redshift measurement and enters into the fitting separately, and each photometric redshift has an associated uncertainty that enters into the total uncertainty on the mass model. Here we calculate the relative magnitudes of the uncertainties from the photometric redshifts and from each galaxy’s shear measurement. For this estimate of the relevance of photometric redshift errors only, we make the approximation that the observed (reduced) shear is approximately equal to the shear  $\gamma$ ,

$$g = \frac{\gamma}{1 - \kappa} \simeq \gamma \quad (10)$$

where  $\kappa$  is the convergence. The shear can be written as

$$\gamma(\theta) = \int \mathcal{D}(\theta - \theta')\kappa(\theta')d^2\theta', \quad (11)$$

(see Bridle et al. 1998), where  $\mathcal{D}$  is the lensing kernel, and  $\kappa$  is the convergence defined in Section 4.1. Using the definition of  $\kappa$  and Eq. 7 one can write

$$\gamma(\theta) = \frac{4G}{c^2} \frac{D_d D_{ds}}{D_s} \int \Sigma(\theta')\mathcal{D}(\theta - \theta')d^2\theta' \quad (12)$$

or

$$\int \Sigma(\theta') \mathcal{D}(\theta - \theta') d^2\theta' = \gamma(\theta) \frac{c^2}{4G} \frac{D_s}{D_d D_{ds}} \quad (13)$$

where the mass model is now isolated on the left-hand side and the observables are isolated on the right-hand side. Uncertainties enter the right-hand side on an equal basis through the estimate of the shear  $\gamma$  and through the distance ratio  $D_{ds}/D_s$  which depends on the source photometric redshift (the distance to the lens  $D_d$  is fixed through spectroscopic redshifts). In our data, the distance ratio uncertainty associated with a typical source galaxy’s photometric redshift measurement is about 30% (expressed as a percentage of its distance ratio). The uncertainty in the shear estimate from *any* source galaxy is much larger,  $>500\%$ , because a typical shear is  $\tilde{0}.05$  and shape noise—the uncertainty floor set by the random orientations of source galaxies—is  $\tilde{0}.25$ . Therefore the per-galaxy distance ratio uncertainty of  $\sim 30\%$  is negligible.

Although we have shown that random photometric redshift errors are negligible on a per-galaxy basis, systematic errors in the photometric redshifts can still cause a bias on the measured cluster masses. To address this question, we performed simulations of photometric redshift errors similar to those in Margoniner & Wittman (2008). We ran multiple realizations tailored to each cluster, starting with the actual DLS catalog for the subfield containing that cluster. For each realization, random photometric zeropoint errors were chosen according to the zeropoint uncertainties in each filter as derived from repeat observations. One of two priors for the distribution of redshift and spectral type as a function of magnitude were chosen: either the HDF prior from Benítez (2000), or the prior from Ilbert et al. (2006). In a given realization, for each galaxy, the  $R$  magnitude was used to choose a random type and redshift following the prior; these were used to generate synthetic colors and photometric noise and zeropoint errors were added. The photometric redshifts were then estimated using BPZ (Benítez 2000), using either of the two priors at random, thus simulating the effect of uncertain knowledge of the prior.

For a given lens, the induced shear scales linearly with the distance ratio  $\frac{D_{ds}}{D_s}$  as shown by Eq. 12. Given the true and estimated redshift for each galaxy in a simulation, the ratio of true to estimated distance ratios was computed, and then averaged over the galaxies in the simulation. This yielded a distance ratio bias for that realization. The uncertainty in distance ratio bias was estimated by taking the rms of thirty realizations for each cluster. The typical bias was 5-10%, with the sign that the true distance ratio was smaller than estimated, which implies that the mass of the cluster is larger than estimated for a given shear. The typical uncertainty in the bias was 1-2%.

We then use the distance ratio bias to “correct” the distance ratio calculated from the source photometric redshifts and the redshift of the cluster in question. The uncertainty

in this bias correction is negligible compared to that from other sources. A simple error propagation from the uncertainty in the correction to the mass estimator shows a  $\sim 1\%$  effect on the mass estimate. The actual uncertainty must be larger because the simulation does not include some real effects, most notably a realistic variety of galaxy spectral energy distributions (SEDs). However, even if the uncertainty in the source redshift bias were doubled or tripled, the loosening of the mass constraints would be trivial, because other uncertainties dominate. At the same time, the 5-10% correction does capture the systematic effects of our filter gaps and photometry noise.

## 5. Results

For the NFW profile, we found that the lensing data provide very little constraint on the concentration parameter  $c$ . We therefore set the parameter to  $c = 5$ , which is a typical value for the masses in question (Seljak 2000; Dolag et al. 2004). Setting the concentration to 6 (a high but reasonable value from Dolag et al. 2004) instead of 5 changes the mass estimates by less than 10%, well within the uncertainty on the mass. When fitting the SIS profile, stability problems due to the divergence in the density at small radii were not an issue, due to the central  $1'$  cut described above. To compare the results from the SIS fit and the NFW fit we convert the SIS  $\sigma_v$  into  $M_{200}$ . They are related by

$$M_{200} = \sqrt{\frac{48}{200\pi\rho_{cr}}} \left(\frac{\sigma_v^2}{2G}\right)^{\frac{3}{2}} \quad (14)$$

where  $\rho_{cr}$  is at the redshift of the cluster.

We refer the reader to the figures presented in Wittman et al. (2006), which show the multiband optical imaging of each candidate, with the convergence maps and X-ray contours overlaid.

### 5.1. Single Profile Fits

The results from the single profile fits, described in Section 4.1 item (i), are presented in Table 2 and Figure 2.

Table 2 shows the resulting masses with  $1\sigma$  errors after applying the prior for the cluster profile center position given in Eq. 9. We also include the offset in arcminutes between the best-fit centre position and the X-ray centre position; the average offset is about 0.4 arcminutes. We find from simple simulations that a mis-center of this magnitude could still

bias the mass estimate by up to 5 per cent. Therefore not applying the prior (Eq. 9) might have been significant for some of the clusters in our sample, given the size of their statistical errors.

The mass found from the SIS profile is similar to the one found from the NFW profile; the two mass estimates agree to well within the  $1\sigma$  level. The mass found for candidate 8 is consistent with the estimate from Wittman et al. (2003) once the shear calibration error in that paper has been corrected, see footnote b in Table 2. Note that the previously published mass estimates for Abell 781 (Sehgal et al. 2008) are not directly comparable to the new results presented in Table 2 because Sehgal et al. (2008) performed simultaneous fitting, not sequential fitting of each clump as in Table 2. We therefore defer a comparison to §5.2, in which we also fit all clumps simultaneously.

Figure 2 presents the results from the single profile fits using the NFW profile. For each candidate  $M_{200}$  with its uncertainty is plotted at the cluster redshift. The uncertainty in the measured mass generally increases with redshift due to the reduction in the number of sources available for the analysis. Candidate 6 has a mass which is consistent with zero, and candidates 3 and 4 have masses which are nearly consistent with zero. This is a curious result for candidates which were selected on the basis of their shear. There are at least four effects at work here:

- The uncertainties here include systematic and not just statistical effects. Thus, a candidate could be *detected* at, say  $3\sigma$ , but with systematic uncertainties its mass estimate may be closer to  $2\sigma$  above zero.
- The fits here marginalize over a range of possible mass centers, whereas the original detections are precisely at the locations with the highest (smoothed) shear value. Noise fluctuations play some role in influencing this location, but at the same time, marginalizing over a large area will artificially lower the mass estimate and increase the uncertainty; see §4.1 for a discussion of these issues. Although we believe we have found a reasonable method for balancing these effects, the end result must be that the cluster mass estimate presented here has lower signal-to-noise than the original detection.
- The original selection was made in the absence of photometric redshift information, while the mass estimates here use that information. Even in the absence of projections, this introduces competing effects: sources at  $z_{\text{phot}} > 1.6$  were thrown away here, thus reducing signal-to-noise if those sources were truly at a reasonably high redshift. At the same time, signal-to-noise will be increased here to the extent that irrelevant sources (at redshifts less than the cluster redshift) can be discarded.

- The use of photometric redshifts may correctly lower the signal-to-noise of projections which are widely enough separated in redshift. Even clusters which are real would have preferentially entered the sample if other groups of galaxies were projected near their line of sight. If the additional groups are at lower redshift, the cluster mass estimate will drop once source redshift information becomes available. If the additional groups are at higher redshift, it would be difficult to eliminate their effect with the simple redshift cut adopted here; they would have to be specifically identified and modeled out. The lowest-mass candidate in this paper, Candidate 6, in particular appears to have a foreground group of galaxies within a projected radius of  $2'$ . Candidate 3 has a foreground group which is much more visible in the images of Wittman et al. (2006), and spectroscopically confirmed at  $z = 0.069$ , but it is at a much larger projected distance ( $5'$ ). A tomographic search making use of source redshift information presumably would not have ranked these candidates so highly. We will present the results of a tomographic search in a future paper.

## 5.2. Simultaneous Multiple-Profile Fits

The results from the multi-profile fit, described in Section 4.1 item (ii), are shown in Table 3. Candidates 4 and 6 only had one X-ray peak so only one profile is fitted, but now the profile center position is set as exactly the X-ray peak position. The masses and  $1\sigma$  uncertainties in Table 3 are quoted after marginalization over the masses of any other clumps within the candidate field.

Figure 3 shows the relationship between the masses from the single profile fit and multi-profile fit, with NFW results at left and SIS results at right. Comparing the two panels, we see that switching from single to multiple fits lowered the SIS mass estimates more than it lowered the NFW mass estimates. This suggests empirically that the NFW profile is less susceptible to shear from the neighboring clumps, a suggestion which is supported mathematically by the greater steepness of the NFW profile at larger radii.

We now examine the effect of single vs. multiple fits on individual clusters. Candidates 1 and 2, with the most X-ray-emitting clumps (four), are the two with significantly lower masses in the multi-profile fit as compared to the single-profile fit. This is simply due to the shear of the neighboring clumps contributing “mass” to the single-profile fit. Candidates 7 and 8, with three and two X-ray-emitting clumps respectively, also have lower masses with the simultaneous-fitting approach, but this effect is not significant given their larger uncertainties. For the remainder, the mass estimates did not decrease with the simultaneous-fitting approach; of these, only Candidate 3 had more than one X-ray-emitting clump. Collectively,



Table 2: Results from single profile fitting

Cluster	z	Centre offset (arcminutes)	NFW Result	SIS result		Published result	No. sources
			$M_{200}$ ( $10^{14} M_{\odot}/h$ )	$\sigma_v$ (km/s)	$M_{200}$ ( $10^{14} M_{\odot}/h$ )	$M_{200}$ ( $10^{14} M_{\odot}/h$ )	
1A	0.302	0.52	$4.2^{+0.6}_{-0.5}$	$900^{+37}_{-40}$	$4.1^{+0.5}_{-0.5}$	$4.4^{+1.6a}_{-1.5}$	49411
1B	0.291	0.34	$4.6^{+0.6}_{-0.5}$	$925^{+42}_{-33}$	$4.5^{+0.6}_{-0.5}$	$3.7^{+2.1a}_{-1.5}$	50456
1C	0.427	0.40	$5.4^{+0.8}_{-1.0}$	$1025^{+49}_{-60}$	$5.6^{+0.8}_{-0.9}$	$4.3^{+2.7a}_{-2.4}$	37648
2	0.296	0.31	$1.8^{+0.4}_{-0.4}$	$700^{+44}_{-55}$	$1.9^{+0.4}_{-0.4}$	-	45249
3	0.267	0.43	$0.6^{+0.3}_{-0.2}$	$400^{+78}_{-109}$	$0.4^{+0.2}_{-0.2}$	-	42743
4	0.190	0.48	$0.4^{+0.2}_{-0.2}$	$225^{+85}_{-141}$	$0.1^{+0.1}_{-0.1}$	-	40991
6	0.427	0.49	$0.4^{+0.2}_{-0.4}$	$300^{+115}_{-206}$	$0.1^{+0.3}_{-0.1}$	-	28626
7	0.530	0.31	$2.2^{+1.0}_{-1.2}$	$800^{+120}_{-118}$	$2.5^{+1.3}_{-0.9}$	-	16354
8	0.680	0.25	$1.8^{+0.8}_{-1.0}$	$725^{+121}_{-134}$	$1.7^{+0.9}_{-0.7}$	$2.8^{+1.0b}_{-1.0}$	19207

<sup>a</sup>Converted from  $M_{500}$  value in Sehgal et al. (2008).

<sup>b</sup>Converted from  $\sigma_v$  in Wittman et al. (2003). Note: We found there was an error in the shear calibration of Wittman et al. (2003). With proper calibration, the weak lensing mass estimates and statistical uncertainties in that paper should be divided by a factor of 1.6. The mass presented here has had this correction applied.

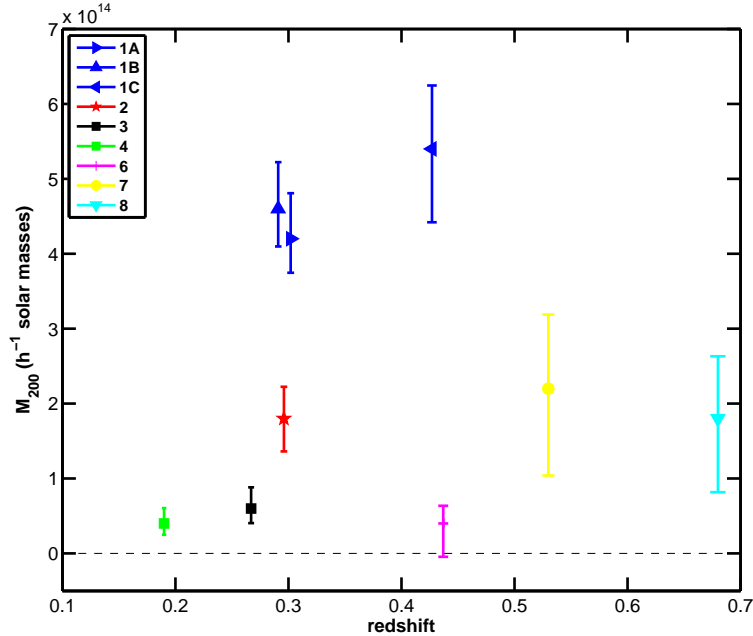


Fig. 2.— Mass from the single NFW profile fit as a function of the cluster’s redshift. See the legend to relate the data points to the candidates.

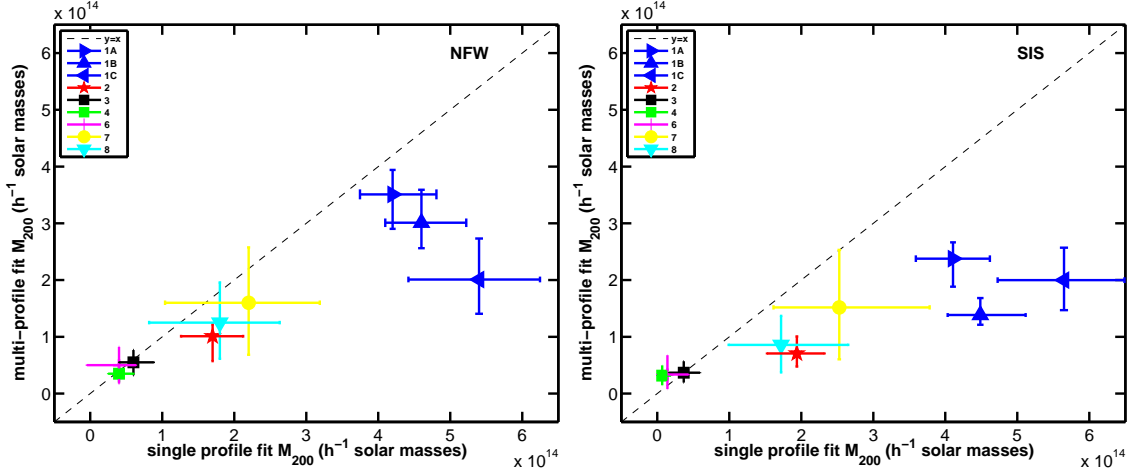


Fig. 3.— Comparison of masses from the single profile fit and the multi-profile fit. The left hand panel shows the results from the NFW profile and the right hand panel shows the results from the SIS profile. See the legend to relate the data points to the candidates. Note that for clarity the candidate 2 result from the NFW profile fit (red/dark star point, left hand panel) has been offset to the left by  $0.1 \times 10^{14} M_{\odot}/h$ , which is much less than the size of its errorbar.

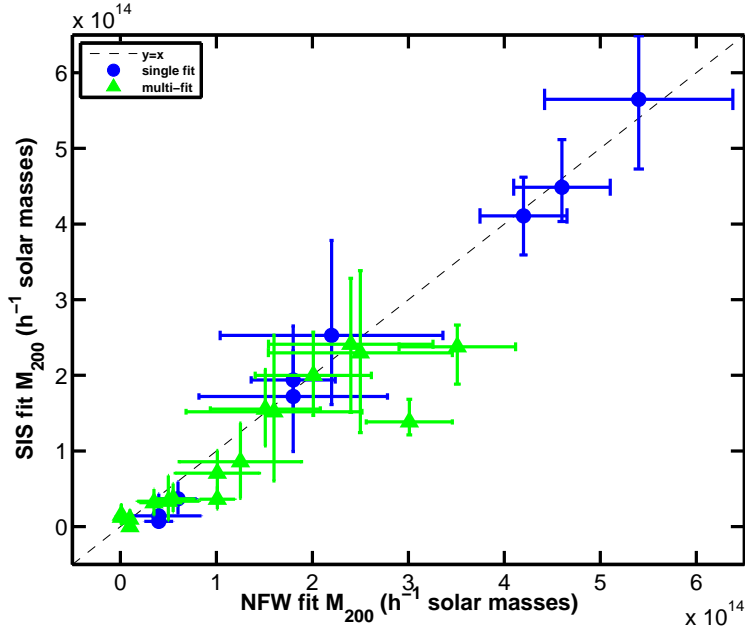


Fig. 4.— Comparison of masses found from fitting the SIS profile and the NFW profile. The green (light) triangle points are the results from the multi-profile fit. The blue (dark) circle points are the results from the single profile fit.

Table 3: Results from multi-profile fitting

Clump	Peak Value	z	NFW		SIS		Published	No. sources
			$M_{200}$ ( $10^{14} M_{\odot}/h$ )	$\sigma_v$ (km/s)	$M_{200}$ ( $10^{14} M_{\odot}/h$ )	$M_{200}$ ( $10^{14} M_{\odot}/h$ )		
1a	0.0188	0.302	$3.5^{+0.4}_{-0.6}$	$750^{+30}_{-57}$	$2.4^{+0.3}_{-0.5}$	$4.4^{+1.6a}_{-1.5}$	48228	
1b		0.291	$3.0^{+0.6}_{-0.4}$	$625^{+43}_{-27}$	$1.4^{+0.3}_{-0.2}$	$3.7^{+2.1a}_{-1.5}$		
1c		0.427	$2.0^{+0.7}_{-0.6}$	$725^{+64}_{-72}$	$2.0^{+0.6}_{-0.5}$	$4.3^{+2.7a}_{-2.4}$		
1d		0.302	$0.0^{+0.5}_{-0.0}$	$300^{+80}_{-120}$	$0.2^{+0.1}_{-0.1}$	-		
2a	0.0151	0.296	$1.0^{+0.2}_{-0.4}$	$500^{+66}_{-66}$	$0.7^{+0.3}_{-0.2}$	-	51738	
2b		0.296	$1.0^{+0.6}_{-0.4}$	$400^{+58}_{-61}$	$0.4^{+0.2}_{-0.1}$	-		
2c		0.296	$1.5^{+0.5}_{-0.6}$	$650^{+68}_{-79}$	$1.6^{+0.5}_{-0.5}$	-		
2d		0.210	$0.0^{+0.4}_{-0.0}$	$275^{+102}_{-126}$	$0.1^{+0.2}_{-0.1}$	-		
3a	0.0136	0.267	$0.6^{+0.2}_{-0.2}$	$400^{+68}_{-86}$	$0.4^{+0.2}_{-0.2}$	-	44680	
3b		0.068	$0.1^{+0.2}_{-0.2}$	$250^{+76}_{-127}$	$0.1^{+0.1}_{-0.1}$	-		
4a		0.190	$0.4^{+0.2}_{-0.2}$	$375^{+69}_{-97}$	$0.3^{+0.2}_{-0.2}$	-	41085	
6a		0.426	$0.5^{+0.3}_{-0.3}$	$400^{+120}_{-188}$	$0.3^{+0.3}_{-0.3}$	-	28632	
7a	0.0119	0.530	$1.6^{+1.0}_{-1.0}$	$675^{+146}_{-214}$	$1.5^{+1.0}_{-0.9}$	-	19357	
7b		0.531	$0.1^{+0.3}_{-0.0}$	$0^{+215}_{-0}$	$0.0^{+0.2}_{-0.0}$	-		
7c		0.530	$2.5^{+1.2}_{-1.0}$	$775^{+117}_{-159}$	$2.3^{+1.1}_{-1.1}$	-		
8a	0.0119	0.680	$1.3^{+0.7}_{-0.6}$	$575^{+113}_{-167}$	$0.9^{+0.5}_{-0.5}$	$2.8^{+1.0b}_{-1.0}$	20289	
8b		0.609	$2.4^{+0.9}_{-0.9}$	$800^{+91}_{-121}$	$2.4^{+0.9}_{-0.9}$	-		

<sup>a</sup>Converted from  $M_{500}$  value in Sehgal et al. (2008).

<sup>b</sup>Converted from  $\sigma_v$  in Wittman et al. (2003), see footnote b in Table 2.

the single-clump candidates saw their masses *increase* slightly with the second approach. Although this is not a very significant effect, it may follow from the one element of the algorithm which changed, namely, that positions are fixed to the X-ray positions rather than marginalized over. The small difference between the two results implies that the X-ray peak position was a good proxy for the cluster center position, and that we did not marginalize over too large an area.

The striking effect of clump multiplicity demonstrates that care must be taken not to introduce a systematic error in the measured cluster masses due to the presence of nearby shear peaks. It also implies that there could be significant systematic errors from nearby undetected masses.

We now compare our results to previously published mass estimates. There is a dramatic change in Candidate 8. Recall the single-profile fit result of  $1.7_{-0.7}^{+0.9} \times 10^{14} h^{-1} M_{\odot}$  presented in Table 2 was higher than, but consistent with, the corrected Wittman et al. (2003) result of  $2.8_{-1.0}^{+1.0} \times 10^{14} h^{-1} M_{\odot}$ . When we simultaneously fit the additional extended X-ray source in the field, the additional source is assigned most of the mass,  $2.4 \pm 0.9 \times 10^{14} h^{-1} M_{\odot}$ , and the main source is left with only  $0.9 \pm 0.5 \times 10^{14} h^{-1} M_{\odot}$ . The reason is unclear: the main source has a larger X-ray flux by a factor of 1.4 despite being at a higher redshift ( $z = 0.68$  vs. 0.61). The dynamical and strong-lensing mass estimates in Wittman et al. (2003) were also consistent with the higher mass, and cannot be affected by the secondary cluster at lower redshift. It could be argued that those estimates do not strongly rule out the lower mass estimate, given the small number of members with spectroscopy (17) and the unknown redshift of the strongly lensed arc. Hence, a complete understanding of this system may require more data, in the form of an arc redshift, *Hubble Space Telescope* imaging for a higher-resolution weak lensing analysis, and/or more spectroscopy.

The second system with previously published mass estimates is Abell 781, for which Sehgal et al. (2008) simultaneously fit NFW profiles to clumps 1a (which they called the “Main” cluster), 1b (which they called the “Middle” cluster), and 1c (which they called the “East” cluster).<sup>2</sup> Our simultaneously-fit NFW masses are consistent with theirs. Although Table 3 gives the impression that the new results are systematically somewhat lower, the total discrepancy of the three clumps is only about one in terms of  $\chi^2$ , for three degrees of freedom. This is not significant. The velocity dispersions inferred from the multiple simultaneous SIS fits also agree with the spectroscopic velocity dispersions measured by Geller et al. (2005).

---

<sup>2</sup>Note that Sehgal et al. (2008) considered cluster 1d to be merging with cluster 1a, and did not fit it separately. We do fit it separately, which should lower the mass of cluster 1a somewhat. Sehgal et al. (2008) also found a “West” cluster in XMM data covering a larger field. We do not consider that cluster here, as its low mass and large projected distance make it unlikely to affect the results.

When the shear fits are not simultaneous (Table 2), the inferred velocity dispersions are significantly overestimated.

Finally, we compare the results between the two different profiles, SIS and NFW, for all the measured masses (Figure 4). Only the masses of candidates 1a and 1b from the multiple profile fit have more than a  $1\sigma$  discrepancy between the two profile types; their SIS masses are lower than their NFW masses by about  $2\sigma$ . When the clumps are not fit simultaneously (blue points), masses inferred from the two profiles are in excellent agreement. Given the greater susceptibility of the SIS to boosting by neighbors, we expect a shift in this direction, but we would have expected the non-simultaneous fits to lie *above* the unity-slope relation rather than *on* it. Given that these are the two highest-shear clumps in the survey, this somewhat unexpected behavior may be indicating that high-mass neighbors induce additional subtle effects not accounted for by merely simultaneous fitting (for example, magnification changing the source redshift distribution).

Figure 4 also suggests that the NFW profile tends to assign more mass to the candidate; nearly all the multiple-profile points lie below the line of unity slope. For the single-profile fits, this effect seems to be nearly cancelled by the tendency of the SIS to pull in more neighboring mass. We investigated this observation with data simulated using an NFW profile. We fitted the data with both SIS and NFW profiles and then compared the masses measured from both profiles. We found instead that fitting the SIS profile caused a slight over-estimation of the true mass, but this was insignificant given the size of the statistical errors. The over-estimation was due to the inner regions of the profile having more weight in the fitting, and in these regions the SIS density is less than the NFW density for the same mass. Therefore it is possible the reason why the NFW profile seems to assign more mass to the cluster than the SIS profile lies within the (unknown) exact details of the true density profile of clusters at these inner radii. This is reasonable because the shape of the cluster density profile at the lowest radii is the most uncertain. The NFW profile is predicted by cold dark matter only simulations, and would be affected at low radii by the baryonic cluster component, the existence of massive neutrinos or even the possibility that the dark matter has a non-zero cross-section.

## 6. Summary and Discussion

We have measured the masses of a sample of shear-selected clusters from the Deep Lens Survey by fitting NFW and SIS profiles to the full dataset of shears and source redshifts. For each type of profile, we fit the data in two different ways: (i) we fit to each *shear peak separately*, marginalizing over likely locations of the mass profile center; (ii) we fit to all the

*extended X-ray sources simultaneously*, fixing the mass profile locations at those of the X-ray peaks. We find that:

- Masses measured with either profile are consistent with each other on a per-cluster basis. This is because the two profiles are similar to each other at the cluster radii probed by the weak lensing. There are hints that the NFW profile tends to assign more mass on average, but a larger and higher-S/N sample would be required to confirm this. The same tendency was found by Okabe et al. (2009), who studied 22 clusters with weak lensing signal measured from Subaru/Suprime-Cam imaging data.
- Fitting multiple clumps simultaneously can yield a much lower mass estimate compared to fitting them separately. This is because the single-profile fit conflates shear from nearby peaks with shear from the peak being fit. The size of this effect was a factor of about 1.5 to 2 for Abell 781 and for Candidate 2.
- Uncertainty in the mass profile center had a relatively small effect here, but should not be overlooked. For the candidates with a single extended X-ray source, the *only* difference between approaches (i) and (ii) was the marginalization over, vs. fixing of, the mass profile center, and the results did not change dramatically. There was a shift in the sense that marginalizing over possible centers did yield lower mass estimates, but it was small compared to the typical per-cluster uncertainty here. While adequate for the current purpose, with larger samples this may become a nontrivial systematic issue. Especially since we find from simplified simulations that a small offset of just 0.4 arcminutes could cause a systematic bias on the mass if the precision of the statistical errors is greater than 5 per cent. More investigation into the typical BCG/X-ray and mass peak position offsets is required to make sure this systematic is fully under control.
- A few clusters have masses which are consistent or nearly consistent with zero. Although several effects may be contributing, the most likely is that the original shear selection, having been done without regard to source redshifts, was vulnerable to line-of-sight projections in a way that the current fitting technique is not. This problem may have been compounded by the heavy smoothing in the Wittman et al. (2006) convergence maps. As shown by the spectroscopy and X-ray detections in Wittman et al. (2006), these are real clusters, but they may be so poor that they passed the selection only because of nearby projections. Tomographic selection should reduce this problem, but, according to the simulations of Hennawi & Spergel (2005), cannot eliminate it. Followup spectroscopy and/or X-ray observations can prove that a cluster exists at that location, but much more extensive (perhaps prohibitive) followup would be required to prove that there are no additional groups projected nearby that boosted

the cluster into the sample. An alternative would be to think of these systems simply as shear peaks rather than clusters, and use the formalism of Wang et al. (2009) or Marian et al. (2008) to constrain cosmology.

Comparing to previous mass estimates of some of these systems, we find that Abell 781 is entirely consistent. However, Candidate 8 is more puzzling than previously thought; the new fits indicate that the secondary X-ray peak has more mass than the primary one. More data may be required to fully understand this system.

Simulations suggest that the ellipticity of clusters could be used as a cosmological probe, if sufficiently good statistics can be obtained (Hopkins et al. 2005; Ho et al. 2006). Observations do suggest that cluster shapes, measured by the distribution of galaxies, X-rays, SZ effect and weak lensing, are usually not spherical. There is also indication that the mean ellipticity evolves with redshift (Melott et al. 2001; Plionis 2002), with clusters becoming less elliptical over time. This is expected because of hierarchical cluster formation and the reduced merger rate as clusters undergo a relaxation process. The systematic ellipticity of cluster dark matter halos was recently detected by stacking hundreds of clusters in SDSS (Evans & Bridle 2009).

An extension to the current paper would be therefore, to allow the individual clumps to be fitted with an elliptical profile instead of an axi-symmetric one. This may reduce the number of clumps required in the fit, or produce more realistic mass estimates for the individual clumps. However the ellipticity of clusters is difficult to measure for individual systems (although see Cypriano et al. 2004) due to the high noise levels on individual shear measurements. Corless & King (2009) looked at the resulting biases on the cluster mass function from fitting a spherical model to both spherical and elliptical (triaxial) halos after stacking the lensing signals of many clusters binned by mass-correlated observables. They fitted a circular model to the stack of elliptical halos and measured  $M_{200}$  in a circular contour and found that this did not match with the  $M_{200}$  values of the original individual halos, if this  $M_{200}$  was calculated in elliptical isodensity contours. However they found that the stacked  $M_{200}$  matched well to the  $M_{200}$  of the individual halos, if the  $M_{200}$  values of the original elliptical halos were defined using circular contours instead, where the density at different points around these circular contours was not constant.

We performed a simulation to test this effect on a per-cluster basis. The clusters in Corless & King (2009) were stacked without attention to aligning their axes, so the random orientations of many halos in each bin would artificially circularise the average of the stacked halos. In our simulations we calculate the difference between (i) the mass obtained from fitting a circular model and (ii) the mass within the circle containing  $200\rho_{crit}$  of the best-fit elliptical model. We find these two numbers are the same to better than 1 per cent accuracy.

Therefore we conclude that there is negligible systematic bias in our results from fitting a spherical profile to an elliptical halo as long as  $M_{200}$  in circular radii is the quantity of interest.

Many different cluster surveys will be taking place in the near future. They will aim to probe the growth of structure over time, beginning a new genre of cosmological analysis. Understanding the sample selection and relating the cluster observables to the mass is a large task. Shear selection in principle eases this task because it is independent of the nature of the matter and of its dynamical state, but there are clearly several issues which must be resolved, principally the observationally difficult task of accounting for projections, but also including determination of the mass profile center without biasing the mass estimate. In the future, large surveys such as the Large-aperture Synoptic Survey Telescope (LSST) will find on the order of 100,000 shear-selected clusters (Tyson et al. 2003). With such massive surveys systematics will become important. The modest samples produced by DLS and other current surveys (Miyazaki et al. 2007; Gavazzi & Soucail 2007; Dietrich et al. 2007) will be the testing ground for developing methods to successfully analyze these new large data sets.

We thank Jim Bosch and Eduardo Cypriano for useful conversations. The DLS has received generous support from Lucent Technologies and from NSF grants AST 04-41072 and AST 01-34753 and NASA grant NNG05GD32G. Observations were obtained at Cerro Tololo Inter-American Observatory and Kitt Peak National Observatory, which are operated by the Association of Universities for Research in Astronomy, Inc., under cooperative agreement with the National Science Foundation. AA acknowledges support from a British Council grant and thanks the University California, Davis for its hospitality during the completion of this work. SB acknowledges support from the Royal Society in the form of a University Research Fellowship.

## REFERENCES

- Battye, R. A., & Weller, J. 2003, *Phys. Rev. D*, 68, 083506
- Benítez, N. 2000, *ApJ*, 536, 571
- Bardeau S., Soucail G., Kneib J.-P., Czoske O., Ebeling H., Hudelot P., Smail I., Smith G. P., 2007, *A&A*, 470, 449
- Bridle, S. L., Hobson, M. P., Lasenby, A. N., & Saunders, R. 1998, *MNRAS*, 299, 895
- Bernstein, G. M. & Jarvis, M. 2002, *AJ* 123, 583



- Bertin, E., & Arnouts, S. 1996, *A&AS*, 117, 393
- Bracewell, R. N. 2000, *The Fourier transform and its applications* / Ronald N. Bracewell. Boston : McGraw Hill, c2000. (McGraw-Hill series in electrical and computer engineering. Circuits and systems),
- Carlstrom, J. E., Holder, G. P., & Reese, E. D. 2002, *ARA&A*, 40, 643
- Clowe D., et al., 2006, *A&A*, 451, 395
- Corless, V. L., & King, L. J. 2009, *MNRAS*, 396, 315
- Cypriano, E. S., Sodré, L. J., Kneib, J.-P., & Campusano, L. E. 2004, *ApJ*, 613, 95
- Dietrich, J. P., Erben, T., Lamer, G., Schneider, P., Schwobe, A., Hartlap, J., & Maturi, M. 2007, *A&A*, 470, 821
- Dolag, K., Bartelmann, M., Perrotta, F., Baccigalupi, C., Moscardini, L., Meneghetti, M., & Tormen, G. 2004, *A&A*, 416, 853
- Evans, A. K. D., & Bridle, S. 2009, *ApJ*, 695, 1446
- Gal, R. R. 2008, *A Pan-Chromatic View of Clusters of Galaxies and the Large-Scale Structure*, 740, 119
- Gavazzi, R., & Soucail, G. 2007, *A&A*, 462, 459
- Geller M. J., Dell'Antonio I. P., Kurtz M. J., Ramella M., Fabricant D. G., Caldwell N., Tyson J. A., Wittman D., 2005, *ApJ*, 635, L125
- Haiman, Z., Mohr, J. J., & Holder, G. P. 2001, *ApJ*, 553, 545
- Hennawi, J. F., & Spergel, D. N. 2005, *ApJ*, 624, 59
- Heymans, C., et al. 2006, *MNRAS*, 368, 1323
- Hoekstra, H., Franx, M., Kuijken, K., & van Dokkum, P. G. 2002, *MNRAS*, 333, 911
- Ho, S., Bahcall, N., & Bode, P. 2006, *ApJ*, 647, 8
- Hopkins, P. F., Bahcall, N. A., & Bode, P. 2005, *ApJ*, 618, 1
- Ilbert, O., et al. 2006, *A&A*, 457, 841
- Johnston, D. E., et al. 2007, *ArXiv e-prints*, 709, arXiv:0709.1159

- Koester B. P., et al., 2007, *ApJ*, 660, 239
- Margoniner, V. E., & Wittman, D. M. 2008, *ApJ*, 679, 31
- Marian, L., Smith, R. E., & Bernstein, G. M. 2009, *PRL*, submitted; arXiv:0811.1991
- Melott, A. L., Chambers, S. W., & Miller, C. J. 2001, *ApJ*, 559, L75
- Miyazaki, S., Hamana, T., Ellis, R. S., Kashikawa, N., Massey, R. J., Taylor, J., & Refregier, A. 2007, *ApJ*, 669, 714
- Muller, G. P., Reed, R., Armandroff, T., Boroson, T. A., & Jacoby, G. H. 1998, *Proc. SPIE*, 3355, 577
- Navarro, J. F., Frenk, C. S., & White, S. D. M. 1997, *ApJ*, 490, 493
- Okabe, N., Takada, M., Umetsu, K., Futamase, T., & Smith, G. P. 2009, arXiv:0903.1103
- Plionis, M. 2002, *ApJ*, 572, L67
- Rosati, P., Borgani, S., & Norman, C. 2002, *ARA&A*, 40, 539
- Rozo, E., et al. 2008, arXiv:0809.2794
- Sehgal, N., Hughes, J. P., Wittman, D., Margoniner, V., Tyson, J. A., Gee, P., & dell'Antonio, I. 2008, *ApJ*, 673, 163
- Seljak, U. 2000, *MNRAS*, 318, 203
- Smith G. P., Kneib J.-P., Smail I., Mazzotta P., Ebeling H., Czoske O., 2005, *MNRAS*, 359, 417
- Tyson, J. A., Wittman, D. M., Hennawi, J. F., & Spergel, D. N. 2003, *Nuclear Physics B Proceedings Supplements*, 124, 21
- Wang, S., Haiman, Z., & May, M. 2009, *ApJ*, 691, 547
- Wittman, D., Tyson, J. A., Margoniner, V. E., Cohen, J. G., & Dell'Antonio, I. P. 2001, *ApJ*, 557, L89
- Wittman, D. M., et al. 2002, *Proc. SPIE*, 4836, 73
- Wittman, D., Margoniner, V. E., Tyson, J. A., Cohen, J. G., Becker, A. C., & Dell'Antonio, I. P. 2003, *ApJ*, 597, 218

Wittman, D., Dell’Antonio, I. P., Hughes, J. P., Margoniner, V. E., Tyson, J. A., Cohen, J. G., & Norman, D. 2006, *ApJ*, 643, 128

Wright, C. O., & Brainerd, T. G. 2000, *ApJ*, 534, 34